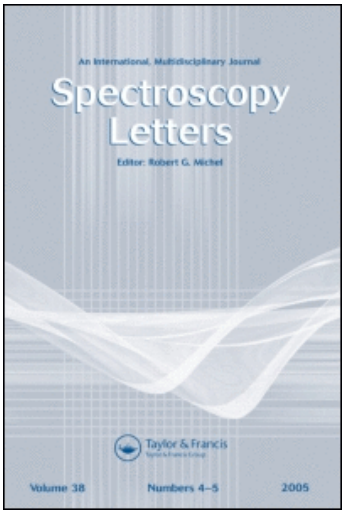

Spectroscopy Letters
Publication details, including instructions for authors and subscription information:
http://www.informaworld.com/smpp/title~content=t713597299

Synthesis and Optical Properties of Eu^{3+} Ion Doped Nanocrystalline Hydroxyapatites

R. J. Wiglusz[a]; A. Bednarkiewicz[a]; A. Lukowiak[a]; W. Strek[a]
[a] Institute of Low Temperature and Structure Research, Polish Academy of Sciences, Wroclaw, Poland

Online publication date: 30 July 2010

To cite this Article Wiglusz, R. J. , Bednarkiewicz, A. , Lukowiak, A. and Strek, W.(2010) 'Synthesis and Optical Properties of Eu^{3+} Ion Doped Nanocrystalline Hydroxyapatites', Spectroscopy Letters, 43: 5, 333 — 342
To link to this Article: DOI: 10.1080/00387010.2010.486716
URL: http://dx.doi.org/10.1080/00387010.2010.486716

Spectroscopy Letters, 43:333–342, 2010

ISSN: 0038-7010 print/1532-2289 online
DOI: 10.1080/00387010.2010.486716

Taylor & Francis
Taylor & Francis Group

Synthesis and Optical Properties of Eu^{3+} Ion Doped Nanocrystalline Hydroxyapatites

R. J. Wiglusz,
A. Bednarkiewicz,
A. Lukowiak,
and W. Strek

Institute of Low Temperature and Structure Research, Polish Academy of Sciences, Wroclaw, Poland

ABSTRACT The $Ca_{10}(PO_4)_6(OH)_2$ hydroxyapatite (HA) nanopowders doped with Eu^{3+} ions were prepared using a wet synthesis method. Their structure and morphology were investigated. The XRD analysis has proven a single-phase of HA nanocrystallites. The average sizes of HA nanocrystallites calcinated at 400°C and 700°C were determined to be about 20 nm and 30 nm, respectively. The emission and excitation spectra as well as the fluorescence decay rates of Eu^{3+} ion doped HA nanocrystallites were measured. Particular attention was given to the spectroscopic properties of Eu^{3+} ions as a luminescent probe of nanocrystalline HA structure as a result of varying annealing temperature and dopant concentration. The Judd-Ofelt analysis of f-f transitions of Eu^{3+}:HA nanocrystallites was performed. The effect of calcination temperatures on grain sizes and luminescence properties is noted and discussed.

KEYWORDS europium ion, hydroxyapatites, nanocrystals, photoluminescence

INTRODUCTION

Recently, a great interest in the optical properties of rare earth doped nanocrystals has been observed due to a number of new phenomena arising from reduced particle volume (size effect).[1–6] On the one hand, the observed reduced density of phonons lead to drastic changes in luminescence spectra (e.g., appearance of hot-bands). On the other hand, an increase of local symmetry for cations in small swelled nanosized grains reduces crystal field strength, modifies Stark level splitting, changes energy levels positions and luminescence spectra shapes. Most of the work concerned dielectric oxides[4–6] and fluoride compounds.[3,7] Spectral properties of the apatites doped with heavy-metals (Pb^{2+} [8]) and rare earth cations (Nd^{3+},[9,10] Yb^{3+},[11,12] and Er^{3+} [13]) have been already studied. However, the investigations were focused mostly on polycrystalline powders and single crystals, considering their applications as luminescent lamp phosphors and as laser hosts.

Doping materials with europium ions provides numerous structural and functional information that help quantify and understand the basic behavior and predict novel applications for these interesting materials. For instance, the $^5D_0 \rightarrow {}^7F_2$ transition being a hypersensitive transition provides information about local chemical environment of the Eu^{3+} ion. Additionally,

Received 21 October 2009; accepted 6 November 2009.

Address correspondence to R. J. Wiglusz, Institute of Low Temperature and Structure Research, Polish Academy of Sciences, P.O. Box 1410, Wroclaw 2, 50-950, Poland. E-mail: R.Wiglusz@int.pan.wroc.pl

the luminescence intensities of $^5D_0 \rightarrow {}^7F_2$ and $^5D_0 \rightarrow {}^7F_4$ scaled by the intensity of $^5D_0 \rightarrow {}^7F_1$ transition, may be used to obtain phenomenological Judd-Ofelt Ω_2 and Ω_4 intensity parameters to quantify the spontaneous emission rates and quantitatively compare these materials with other compounds.[14]

The apatites are inorganic compounds with a general formula $M_{10}(XO_4)_6Y_2$, where M represent divalent cations (e.g., Ca^{2+}, Sr^{2+}, Ba^{2+}, etc.), $XO_4 = PO_4^{3-}$, VO_4^{3-}, AsO_4^{3-}, etc., and Y represent anions: F^-, OH^-, Cl^-, Br^-, $\frac{1}{2}\ CO_3^{2-}$, $\frac{1}{2}\ O^{2-}$, $\frac{1}{2}\ S^{2-}$, etc., respectively. The hexagonal structure in apatites belongs to $\mathbf{P6_3/m}$ space group (Fig. 1) and allows the cations to localize in the 4(f) and 6(h) positions[15] and are able to accommodate a variety of univalent cations as substituents. In that case, charge compensation, proposed by Martin et al.[16] allows to explain with a simple mechanism substitution of divalent calcium ions to trivalent lanthanide ions in hydroxyapatite.

It is worth mentioning that apatites themselves, such as calcium hydroxyapatites $Ca_{10}(PO_4)_6(OH)_2$, are biocompatible and are natural construction materials for bones and teeth.[17] This features combined with highly photostable luminescent properties of rare earth dopants, make the nanocrystalline apatites highly attractive as luminescent bio-labels.[18] However, these materials have not been extensively synthesized or examined in nanocrystalline form,[19] which is a prerequisite for being internalized by cells for bio-imaging or sensing applications. The low temperature synthesis route of Eu^{3+} doped apatites proposed by Doat et al.[18] has led to poor crystalline state of nanoparticles manifested in broad emission bands.

The aim of the present work was to optimize synthesis of well-crystallized Eu^{3+} doped nanocrystalline $Ca_{10}(PO_4)_6(OH)_2$ hydroxyapaptite (HA) and to study their optical properties as a function of nanoparticle size and dopant concentration.

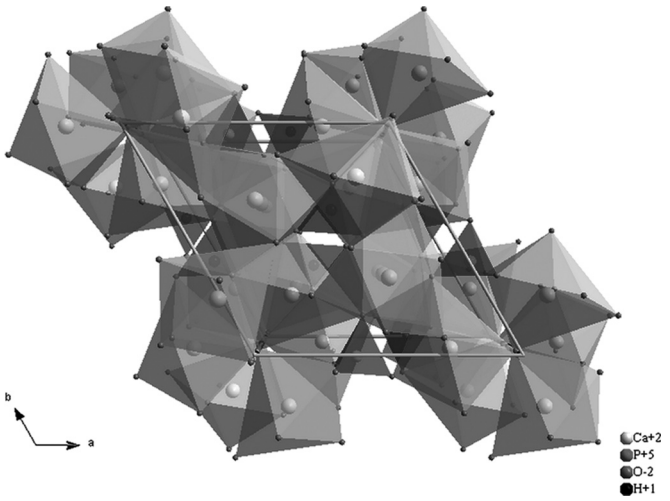

FIGURE 1 The crystal structure of $Ca_{10}(PO_4)_6(OH)_2$ with space group P 63/m (No. 176).

EXPERIMENTAL

Synthesis

The nanocrystalline powders of Eu^{3+} doped hexagonal hydroxyapatites ($Eu{:}Ca_{10}(PO_4)_6(OH)_2$) were prepared by an aqueous synthesis route. Concentration of the optically active Eu^{3+} ions has been set to 1, 3, and 5 mol% in respect to the appropriate Ca^{2+} molar content. Analytical grade Eu_2O_3, $(NH_4)_2HPO_4$, $Ca(OH)_2$, and HNO_3 were used as the starting materials. In this method, stoichiometric amounts of these compounds were taken and mixed into a homogeneous solution with deionized water. It has been well demonstrated that an aqueous synthesis of hydroxyapatites offers considerable advantages over other methods, by providing ability of good mixing of the starting materials and excellent chemical homogeneity of the product. The major limitation of the aqueous route was found to be very low solubility of the calcium hydroxide in the distilled water and low reactivity of the phosphorus compounds, but effective control of pH allowed to solve these problems.

XRD and TEM Analysis

In order to check the development of the crystalline phases, XRD patterns of the prepared materials were obtained from powders, after heating raw mixture at the temperature range of 400 to 700°C for 8 h. The XRD patterns were collected at room temperature on a Stoe STADI P transmission diffractometer in Debye Scherrer geometry (Cu $K\alpha_1$: 1.54060 Å) equipped with a linear position sensitive detector. The XRD patterns were assigned using the Joint Committee on Powder Diffraction Standards (JCPDS) database and the Inorganic Crystal Structure Database (ICSD). The Scherrer's relation, Eq. (1), was used

to estimate the crystallites size:[20]

$$D = \frac{0.9\lambda}{\cos\theta\sqrt{\beta^2 - \beta_0^2}} \quad (1)$$

where D is an average crystallite size, λ denotes the X-ray radiation wavelength, β represents a fullwidth at half-maximum of a diffraction line located at θ and β_0 represents a scan aperture of the diffractometer.

The microstructure of the samples was examined with a Philips CM20 SuperTwin transmission electron microscope (TEM), which provides a resolution of 0.25 nm at 200 kV.

Spectral Measurements

Emission spectra were measured with a Jobin-Yvon THR1000 spectrophotometer equipped with Hamamatsu R928 photomultiplier and 1200 l/mm grating blazed at 500 nm. As the excitation source, pulsed (10 Hz) 3rd harmonics (355 nm) of Nd:YAG laser was used. The spectrophotometer exhibits relatively flat response in the spectral range of interest. The excitation spectra ($\lambda_{mon} = 574.4$ nm) were measured with Spectra Pro 750 system. The 450 W xenon arc lamp was used as an excitation source. It was coupled with 275 mm excitation monochromator, which used a 1800 l/mm grating blazed at 250 nm. Emission spectrophotometer was equipped with 1800 l/mm grating blazed at 500 nm. Excitation spectra have been corrected for the excitation light intensity.

Emission lifetimes were measured at 616 nm (under 355 nm excitation, 3rd harmonic of Nd:YAG laser, LOTIS TII with Harmonic Generators for Nd:YAG lasers HG-TF, Belarus) using a Jobin-Yvon THR 1000 spectrophotometer, a Hamamatsu R928 photomultiplier as a detector and a digital oscilloscope Tektronix TDS 380 for data collection. The decay curve fitting was performed with single decay model in Origin 7.5 software.

RESULTS AND DISCUSSION

XRD and TEM Analysis

The XRD pattern of the pure hexagonal structure for $Ca_{10}(PO_4)_6(OH)_2$ doped with Eu^{3+} ion is essentially the same as that found in the literature (hexagonal – ***P63/m*** (176) – ICSD-26204) (see Figs. 1 and 2).[15] The selected XRD patterns for the nanocrystalline hexagonal hydroxyapatites $Ca_{10}(PO_4)_6(OH)_2$ with different Eu^{3+} ions concentration are shown in Fig. 2.

The samples sintered at the temperature range from 400 to 700°C and doped with different concentration of Eu^{3+} ion were characterized by the average sizes of crystallites estimated by Scherrer's equation from broadening of XRD peaks. The particle size was determined to be ≈20 nm for the sample treated at 400°C and ≈30 nm for 700°C, respectively. The average particles size versus dopant concentration and annealing temperature is presented in Table 1. Basically, the average particle size increases with the increase of the annealing temperature and increases with increasing Eu^{3+} ions concentration. Transmission electron microscopy (TEM) was performed to determine morphology and crystallite size of $Ca_{10}(PO_4)_6(OH)_2$ doped with europium ions (see Fig. 3). It disclosed aggregates of nanoparticles with grain size of about 20–50 nm, because of nanoparticles of HA crystallize in the shape of the plates (see Fig. 3b). These results show that values calculated by Scherrer's equation are consistent with that observed by TEM technique.

Emission and Excitation Spectra

The excitation spectra of Eu:$Ca_{10}(PO_4)_6(OH)_2$ materials annealed at 400 to 700°C were monitored

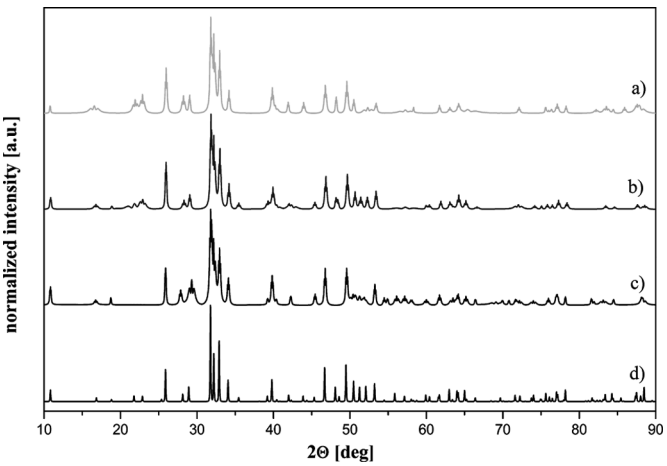

FIGURE 2 **The XRD patterns of $Ca_{10}(PO_4)_6(OH)_2$ prepared at different temperatures by the aqueous synthesis; (a) experimental pattern of 5% Eu:$Ca_{10}(PO_4)_6(OH)_2$ at 600°C, (b) experimental pattern of 3% Eu:$Ca_{10}(PO_4)_6(OH)_2$ at 600°C, (c) experimental pattern of 1% Eu:$Ca_{10}(PO_4)_6(OH)_2$ at 400°C, (d) theoretical pattern of $Ca_{10}(PO_4)_6(OH)_2$, hexagonal – P 63/m (176) – ICSD-26204.**

TABLE 1 The Average Grain Sizes (ø [nm]) and Standard Deviations (SD; Measured from 2 or 3 Different XRD Peaks) of Nanocrystallites as a Function of the Annealing Temperature and the Concentration of Eu^{3+} Ions

T	1%		3%		5%	
[°C]	Ø [nm]	SD [nm]	Ø [nm]	SD [nm]	Ø [nm]	SD [nm]
400	23,3	1,0	20,8	1,0	30,0	3,7
500	21,0	5,2	26,3	7,1	26,2	1,1
600	23,4	9,7	23,4	7,1	24,1	4,6
700	25,5	4,8	28,5	4,1	31,5	4,9

at 574.4 nm with the excitation ranging from 220 to 500 nm. All the spectra were normalized to $^7F_0 \rightarrow {}^5D_2$ transition. Besides a group of sharp Eu^{3+} lines

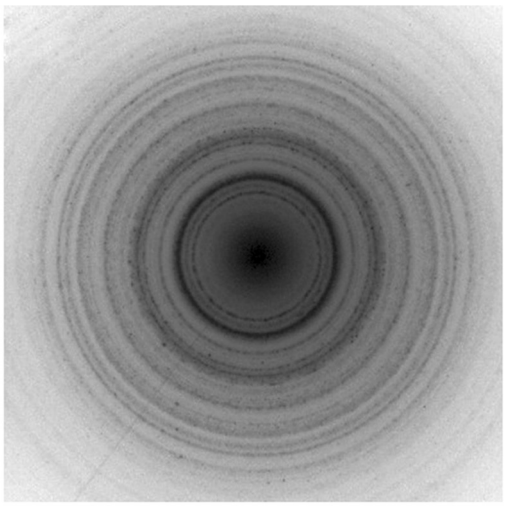

(a)

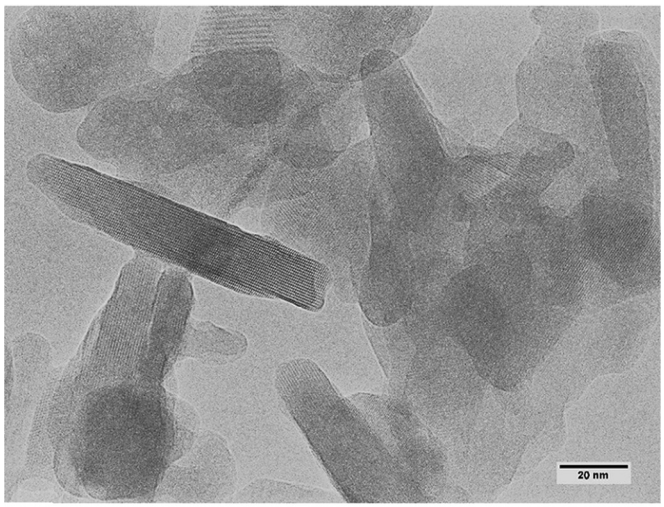

(b)

FIGURE 3 SAD (a) and TEM (b) images of selected $Ca_{10}(PO_4)_6(OH)_2$ material prepared at 600°C.

(Fig. 4), the broad bands have been observed and derived from the $Eu^{3+} \leftrightarrow O^{2-}$ of PO_4^{3-} charge transfer (CT) transitions. These transitions correlates quite well with the optical electro-negativities of the PO_4^{3-} group and Eu^{3+} ion. The energy of this transition is located at ≈320 nm for samples annealed at 400°C. As one may note, the CT position exhibits a blue shift to ≈300 nm with increasing the size of HA nanocrystals. The $Eu^{3+} \leftrightarrow O^{2-}$ CT shift can be explained by the different electronic configuration of the Ca^{2+} and Eu^{3+} and also two different positions of Eu^{3+} ions (site A and B) in the structure of hydroxyapatites.

The emission spectra were investigated for Eu:HA nanocrystallites prepared at different sintering temperatures. They were recorded in the spectral range from 570 to 720 nm under pulsed 355 nm excitation at 300 K and 77 K, respectively (Fig. 5). All the spectra have been normalized to the most intense peak of the $^5D_0 \rightarrow {}^7F_2$ transition. The trivalent europium (Eu^{3+}) has been already studied in apatites.[21,22] Non-degenerate $^5D_0 \rightarrow {}^7F_0$ transition has been used to probe local crystallographic symmetry, number of sites, and site distribution of this cation in the crystalline matrix. Spectral properties of strontium and calcium doped hydroxyapatites studied by means of Eu^{3+} doping as local environment probe, has revealed unusual behavior.[22,23] The abnormal strong intensity for the forbidden $^5D_0 \rightarrow {}^7F_0$ transition was recorded, which was explained by the large contribution of the $4f^5\ 5d^1$ configuration wave functions into the $4f^6$ configuration. Also unusually high energy of the $^5D_0$ (≈17412 cm^{-1}) and $^5D_1$ (18868 cm^{-1}) levels, much above the values reported for other Eu^{3+} doped crystalline and glass compounds, was observed. Additionally, large splitting and overlap of the Stark components of $^7F_1$ (151–1148 cm^{-1}) and $^7F_2$ (747–1624 cm^{-1}) levels[22] indicated the presence of a high and asymmetric crystal field resulting in the mixing of the $^7F_1$ and $^7F_2$ states. This in turn should significantly reduce the forbidden $^5D_0 \rightarrow {}^7F_2$ transition occurrence which, however, is not the case here. Finally in Ref.[23] also emission lines' broadening (50 to 100 cm^{-1} full width at half maximum) was observed and explained by random arrangement of oxygen and vacancies which occur on the axis of channels.

In the hexagonal system, which space group is $P6_3/m$, the $Ca_{10}(PO_4)_6(OH)_2$ presents two kinds of cationic sites. The M(I) site has a trigonal point

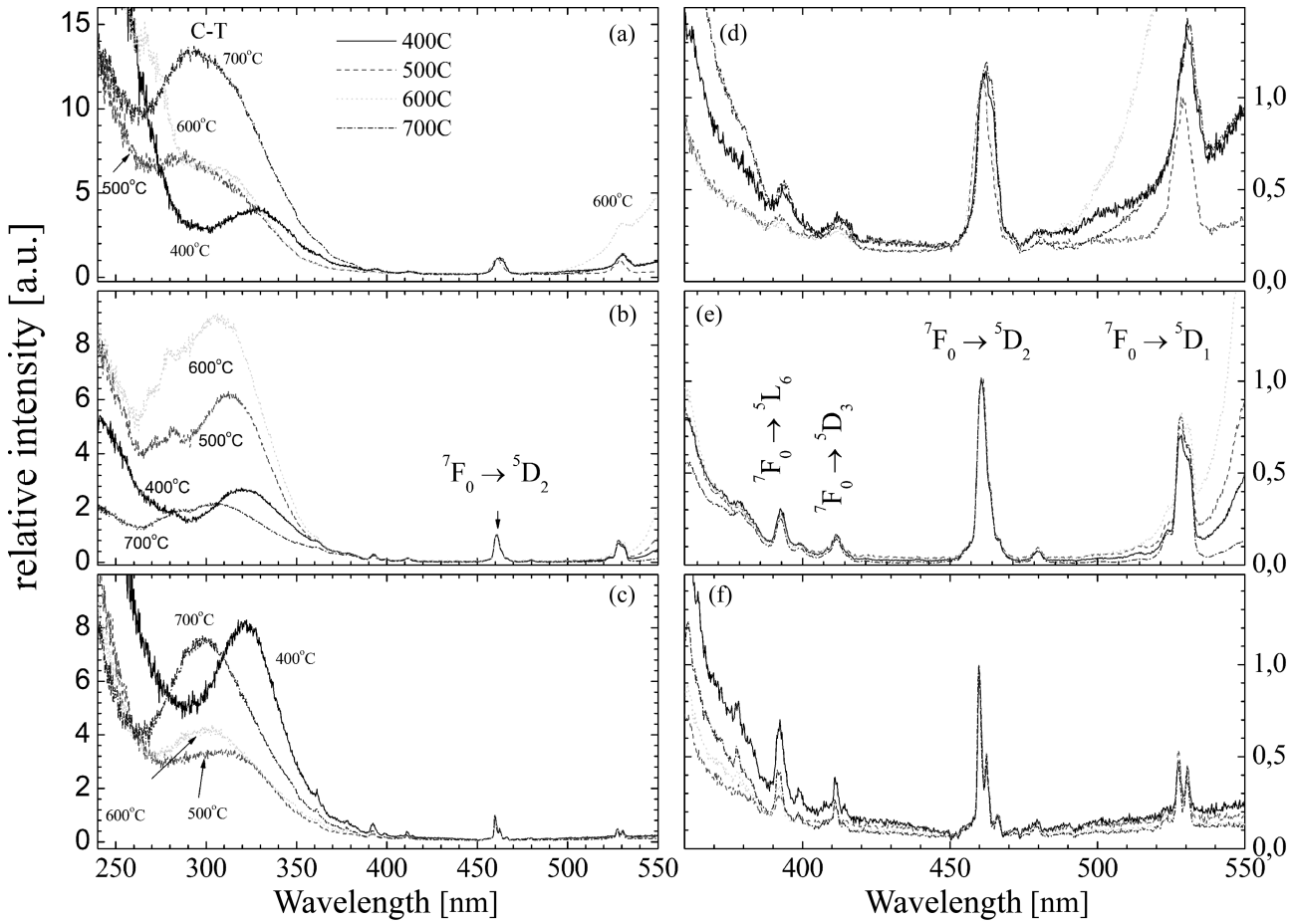

FIGURE 4 The excitation spectra of nanocrystalline $Ca_{10}(PO_4)_6(OH)_2$ doped with 1% Eu^{3+} (a and d), 3% Eu^{3+} (b and e) or 5% Eu^{3+} (c and f) presented versus annealing temperature.

symmetry ($\boldsymbol{C_3}$) corresponding to the 4f site, and it is formed by nine oxygen atoms belonging to the phosphate groups surrounding the cationic site. The M(II) site, which the local symmetry is $\boldsymbol{C_s}$, corresponds to the 6h positioning a sevenfold coordination with six oxygen atoms belonging to phosphate groups and one OH anion.[21] It can be seen that the emission spectra of Eu:$Ca_{10}(PO_4)_6(OH)_2$ nanocrystalline phosphors (Fig. 5) exhibit only the $^5D_0 \rightarrow {}^7F_J$ (J = 0.4) transitions arising from the Eu^{3+} ions, with the dominant $^5D_0 \rightarrow {}^7F_2$ hypersensitive transition located at 15900 to 16400 cm^{-1}. The transitions $^5D_0 \rightarrow {}^7F_3$ and $^5D_0 \rightarrow {}^7F_4$ are observed at around 15300 and 14300 cm^{-1}, respectively. Number of luminescence components is twice larger than the theory predicts for the $0 \rightarrow 2$ transition. The same is true for the $^5D_0 \rightarrow {}^7F_0$ forbidden transition. According to the literature,[21,22] in our samples, the Eu^{3+} ions substitute Ca^{2+} ions and occupy mainly the Ca(II) sites, with relative abundance of 60%. The intense $^5D_0 \rightarrow {}^7F_0$ emission band at ≈17426 cm^{-1} (A sites) is related to this substitution, while the weak band at ≈17317 cm^{-1} (B site) is attributed to the substitution on Ca(I) sites demonstrating relative abundance of 40%. The relative abundance of the A and B sites in our samples was found to vary with both Eu^{3+} doping and sintering temperature.

Luminescence Decays

The luminescence decays of Eu:$Ca_{10}(PO_4)_6(OH)_2$ nanocrystals (see Fig. 6) were fitted with the biexponential model $y(t) = a_1 \exp(-t/\tau_1) + a_2 \exp(-t/\tau_2)$, where a_1 and a_2 indicate relative contribution of short (τ_1) and long (τ_2) decay time components related to two different Eu^{3+} sites. We have found that the longer decay time τ_1 was estimated to be ca. 2 ms whereas the second decay time τ_2 was much shorter ca. 1 ms. One may find a decrease of $a_1/(a_1 + a_2)$ with the annealing temperature increase.

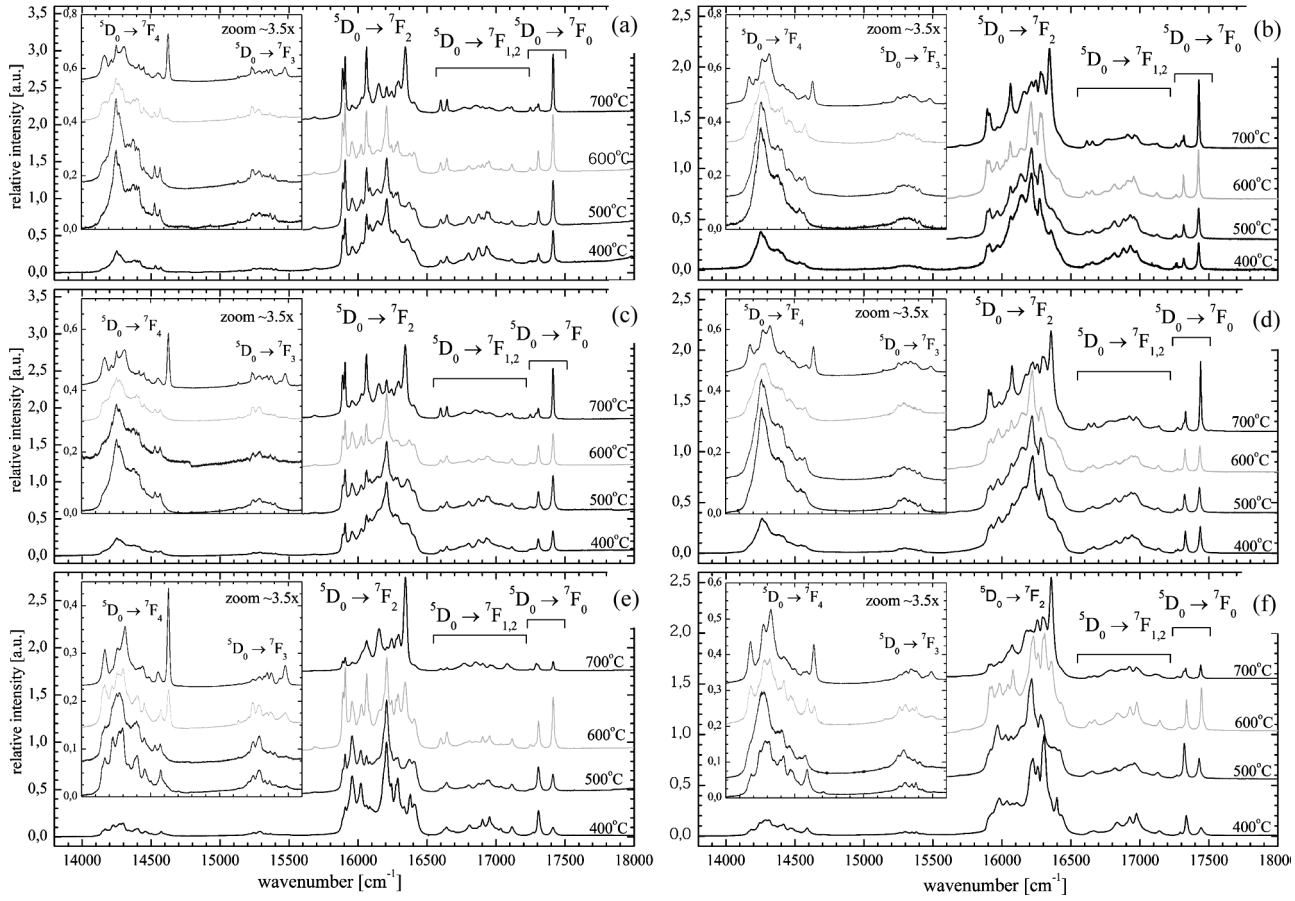

FIGURE 5 **Luminescence spectra at 77 K spectra (left column, a, c, and e) and at 300 K spectra (right column b, d, and f) measured for 1% (first row, a and b), 3% (middle row, c and d) and 5% (bottom row, e and f) Eu^{3+} doped $Eu:Ca_{10}(PO_4)_6(OH)_2$.**

This interesting behavior made us study and find a coherent relation between relative amounts of Eu^{3+} located in the site B and the relative amplitude of short component of the luminescence lifetimes (see Fig. 7). The relative amounts of Eu^{3+} located in site B was calculated as a ratio of luminescence intensity for the site B (integration in 17200 to 17360 cm^{-1} spectral range) to the luminescence intensity of the sites A and B taken together (integration of the $^5D_0 \rightarrow {}^7F_0$ transition at 17200 to 17500 cm^{-1}). The contribution of the short luminescence decay component $(a_1/(a_1 + a_2))$ was obtained in the course of decays fitting with double exponential model. The observed relation suggests that the double exponential decays recorded for $^5D_0$ luminescence come purely from Eu^{3+} ions located at two sites and not from the ion-ion interaction. The sintering temperature increase leads to depreciation of site B occupation, and this can be observed as a decrease of both relative luminescence intensity and the amplitude of short decay component. It is interesting to note that the increase of Eu^{3+} concentration increases the relative intensity of the B site luminescence, while the decay rates are not affected very much.

At room temperature, the increase of annealing temperature leads to slight elongation of short component and decrease of long luminescent lifetime component. Significantly smaller radiative rates and lower quantum efficiencies derived from Judd-Ofelt analysis (see next section) for lower annealing temperatures (smaller grain sizes) are presented in Table 2. A presence of non-radiative depopulation mechanisms pronounced for Eu^{3+} ions exposed to out-of-grain environment is indicated. In opposite to 300 K measurements, the measurements carried at 77 K do not allow correlate the increased grain size with the enhanced luminescence decay (Fig. 6a) as one could expect. Additionally, the low temperature decays cannot be easy related with dopant concentration (Fig. 6a), which makes the interpretation difficult and non equivocal. Moreover,

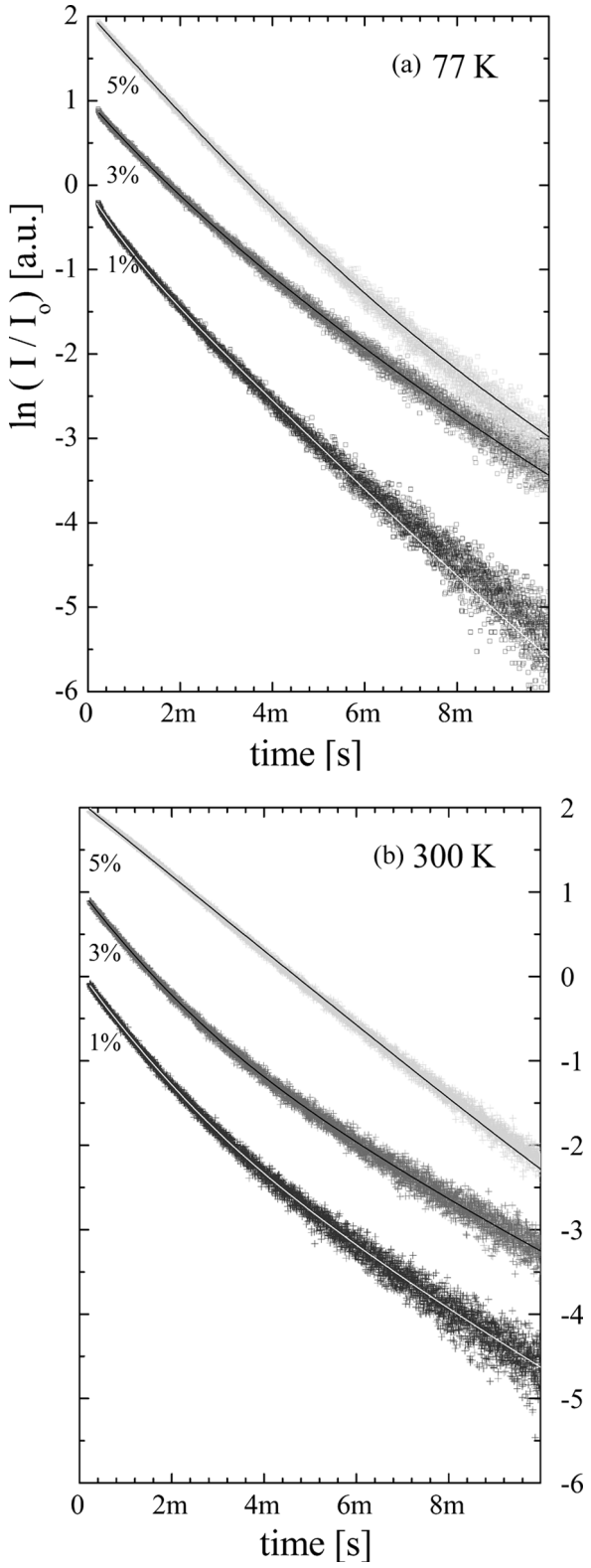

FIGURE 6 **The decay curves obtained for a concentration series samples annealed at 600°C and measured at 77 K (a) and 300 K (b).**

while short decay components observed at 300 and 77 K are similar, the long decay component is surprisingly shorter with 77 K in comparison with 300 K.

Judd-Ofelt Analysis

To get some more insight into the nature of the luminescence behavior of Eu^{3+} ions in nanocrystalline $Eu:Ca_{10}(PO_4)_6(OH)_2$ powders, the Judd-Ofelt model was applied for determination of spontaneous emission coefficients. The intensity parameters $\boldsymbol{\Omega_2}$ and $\boldsymbol{\Omega_4}$ were determined from luminescence spectra following the method described by Kodaira et al.[14] Due to zeroing of adequate $U^{(\lambda)}$ matrix elements and matrix element $U^{(6)}$ being close to zero for the $^5D_0 \rightarrow {}^7F_6$ transition ($U^{(6)} = 0.0005$), the spontaneous emission coefficient $A_{0\text{-}\lambda}(\lambda = 0.6)$ is reduced to

$$A_{0-\lambda} = \frac{64\pi^4 \overline{v}^3 e^2}{3h} \cdot \frac{1}{4\pi\varepsilon_0} \cdot \chi \cdot \Omega_\lambda \cdot \left\langle {}^5D_0 \middle\| U^{(\lambda)} \middle\| {}^7F_\lambda \right\rangle^2 \quad (2)$$

where $\bar{\nu}$ [cm^{-1}] is the energy of the $^5D_0 \rightarrow {}^7F_J$ transition (J = 0.6). The *e, h* and ε_0 constants have their typical meaning and λ equals to 2 or 4 for $^5D_0 \rightarrow {}^7F_2$ or $^5D_0 \rightarrow {}^7F_4$ transitions, respectively. The matrix elements are equal to $\langle {}^5D_0 || U^{(2)} || {}^7F_2 \rangle^2 = 0.0032$ 0.0032 and $\langle {}^5D_0 || U^{(4)} || {}^7F_4 \rangle^2 = 0.0023$.[24] The local field correction factor for emission is expressed as $\chi = n(n^2+2)^2/9$. The index of refraction value was assumed to be $n = 1.651$.

The relation between the integral transition intensity $I_{O\text{-}J}$, the transition energy $h\nu_{O\text{-}J}$, spontaneous emission coefficient $A_{O\text{-}\lambda}$ and $^5D_0$ level population N is expressed as $I_{O\text{-}J} = h\nu_{O\text{-}J} A_{O\text{-}J} N$. Comparison of the relation for both the $^5D_0 \rightarrow {}^7F_2$ and $^5D_0 \rightarrow {}^7F_4$ transitions versus $^5D_0 \rightarrow {}^7F_1$ transition allows recasting the expression for $A_{O\text{-}\lambda}$ as

$$A_{0-\lambda} = A_{0-J} = A_{0-1} \cdot \frac{I_{0-J}}{I_{0-1}} \cdot \frac{\overline{\nu_{0-1}}}{\overline{\nu_{0-J}}} \quad (3)$$

Due to the magnetic character of $^5D_0 \rightarrow {}^7F_1$ transition and its weak dependence on crystal field effect, the $A_{O\text{-}1}$ coefficient was calculated to be 36.5 s^{-1}. This value comes from considering the refractive index of HA after De Sa et al.[25] A knowledge of A_{0J} allows deducing Ω_λ (L=J) from Eq. 2.

The radiative decay rate $A_{JJ'r}$ (J = 0,1,2,3, J′ = 0.6) is equal to

$$A_{JJ'r} = \sum_{J'=0.6} A_{J-J'} = \sum_{J'=0.6} \frac{64\pi^4 \overline{v}^3 e^2}{3h} \cdot \frac{1}{4\pi\varepsilon_0} \cdot \chi \cdot \sum_{\lambda=2,4,6} \Omega_\lambda \cdot \left\langle {}^5D_0 \middle\| U^{(\lambda)} \middle\| {}^7F_\lambda \right\rangle^2 \quad (4)$$

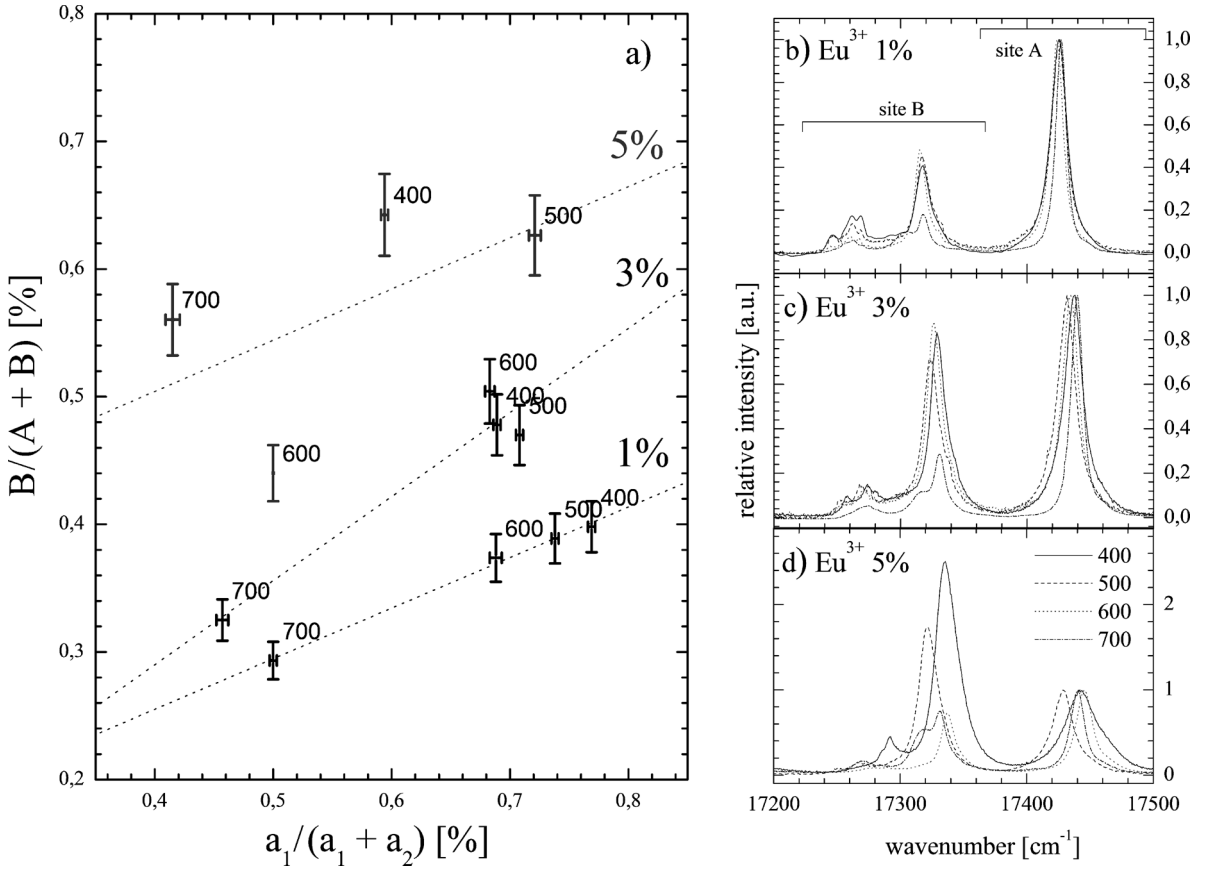

FIGURE 7 **A correlation between biexponential luminescence decays and the emission derived from $^5D_0 \rightarrow {}^7F_0$ transition at different concentration of Eu^{3+} ion and annealing temperatures.**

Since all the $<U^{(6)}>^2$ matrix elements for transitions starting from ^5D_J (J = 0,1,2, and 3) are zero,[26] then only the Ω_2 and Ω_4 parameters are used for calculation of radiative transition rates. For most materials doped with Eu^{3+}, the major contribution to $^5D_0$ level emission arises from the two $^5D_0 \rightarrow {}^7F_2$ and $^5D_0 \rightarrow {}^7F_4$ transitions. For hydroxyapatites however, the $^5D_0 \rightarrow {}^7F_1$ plays the major role therefore the radiative decay rates $A_{0J'r}$ may be expressed as:

$$A_{0J'r} = \sum_{J'=0.6} A_{0-J'} = A_{0-1} + A_{0-2} + A_{0-4} \qquad (5)$$

TABLE 2 **The Decay Rates of Radiative (A_{rad}) and Nonradiative (A_{nrad}) Processes of $^5D_0 \rightarrow {}^7F_J$ Transitions and Intensity Parameters (Ω_2, Ω_4) Determined from Luminescence Spectra of Eu:$Ca_{10}(PO_4)_6(OH)_2$ Nanopowders**

Concentration [%]	Annealing temperature [°C]	A_{rad} [s^{-1}]	A_{nrad} [s^{-1}]	τ_{AVE} [ms]	Ω_2 [10^{-20} cm^2]	Ω_4 [10^{-20} cm^2]	η [%]
1	400	146.1	305.1	2.22	8.13	5.72	32.4
	500	138.0	319.3	2.19	7.58	5.19	30.2
	600	210.2	279.6	2.04	10.18	5.07	42.9
	700	270.0	169.1	2.28	12.50	5.30	61.5
3	400	197.4	241.8	2.28	10.75	7.24	44.9
	500	183.4	264.8	2.23	9.91	6.56	40.9
	600	253.4	183.2	2.30	11.83	5.18	58.0
	700	259.2	150.8	2.44	11.62	4.30	63.2
5	400	231.0	228.8	2.18	10.66	4.46	50.2
	500	245.5	199.2	2.25	11.93	6.00	55.2
	600	202.7	230.5	2.31	9.20	3.59	46.8
	700	244.6	180.8	2.35	12.18	6.57	57.5

Similar equations may be basically written for other ${}^5D_J$ levels. One can also compare the radiative decay coefficient with that experimentally measured A_e and according to Eq. (6) calculate the non-radiative transition coefficients (A_{nr}).

$$A_e = \frac{1}{\tau} = A_r + A_{nr} \tag{6}$$

Finally one can also determine the quantum efficiency of overall luminescence as

$$\eta = \frac{A_r}{A_r + A_{nr}} \tag{7}$$

In spite the luminescence decays *I(t)* exhibit double exponential behavior, for J-O analysis and radiative decay coefficient was derived from averaged luminescence decays calculated as

$$\overline{\tau_{AVE}} = \int t \cdot I(t)dt \Big/ \int I(t)dt \tag{8}$$

One should also mention about the factors influencing the accuracy of the method. In spite of the fact the bands under considerations are relatively close to each other, luminescence spectra corrected for spectral response of the photomultiplier (PM) must be used for quantitative band intensities ratio. The second factor is accuracy of band intensity computation. Choosing slightly different integration region, non-ambiguous baseline shape results in up to 10% of error in band intensity $\int \varepsilon(\upsilon)$. The third factor is a barycentre $\bar{\nu}$ [cm^{-1}] of the band under consideration, which was computed with $\bar{\upsilon} = \int \upsilon \cdot \varepsilon(\upsilon)d\nu / \int \varepsilon(\upsilon)d\nu$ equation from luminescence spectrum $\varepsilon(\nu)$. As one may see on the emission spectra, the distribution of ${}^5D_0 \rightarrow {}^7F_2$ band is heterogeneous and varies for different annealing temperatures and different doping concentrations. The error for omega parameters calculated from total differential of the equations 2 and 3 combined together is equal to $d\Omega/\Omega = \sum dP_i/P_i$, where P_i are measurement dependent parameters, namely $I_{0\text{-}J}$, $I_{0\text{–}1}$, $\overline{\upsilon_{01}}$, $\overline{\upsilon_{0J}}$. Assuming 5% error for each of the factors one obtains $d\Omega/\Omega = 20\%$.

The values of the Ω_2 and Ω_4 parameters as well as other quantities derived from the analysis of luminescence spectra of Eu^{3+}:HA nanocrystals are listed in Table 2.

One may note the Ω_2 parameter basically increases with the annealing temperature, while the Ω_4 parameter slightly falls down for 1% sample with the annealing temperature and looses this correlation for higher doping levels. The Ω_2 parameters are around twice higher than the corresponding Ω_4 parameters. High value of the Ω_2 parameter indicate highest hypersensitive behavior of the ${}^5D_0 \rightarrow {}^7F_2$ transition. These results indicate that larger grains (due to increased annealing temperature) are characterized by more polarizable environment and in result the charge within the unit crystallographic cell is not fully compensated. Furthermore, two different positions of Eu^{3+} ions (site A and B) in the structure of hydroxyapatite indicate that Eu^{3+} ions have two different local environments and the hydroxyapatite structure is formed, the calcinations temperature used is sufficient to allow the embedding of the Eu^{3+} ions inside of the crystallites.

CONCLUSIONS

In the present work we have reported the synthesis and luminescence properties of Eu^{3+} doped HA nanocrystallites. We have found that the aqueous synthesis of Eu:HA nanocrystals allows to obtain well crystallized grains, ranging in size between 20 and 30 nm. The temperature and conditions of synthesis using a wet method did allow for formation of hydroxyapatite phase. The XRD patterns indicated that samples heated at the temperature from 400 to 700°C presented almost complete crystallization of hydroxyapatite phase. The luminescence and excitation spectra of Eu:HA nanocrystals have demonstrated an existence of two major Eu^{3+} sites. We have found that the CT states blue shifts with increasing the size of HA nanograins. The luminescence decays of Eu:HA nanocrystals were fitted by biexponential model assuming a contribution of two different Eu^{3+} sites. The decay rates were significantly faster and quantum efficiencies were lower for smaller grain sizes.

ACKNOWLEDGEMENT

The financial support from Polish Ministry of National Education under grant No. N N507 584938 is gratefully acknowledged.

REFERENCES

1. Malyukin, Y.V.; Masalov, A.A.; Zhmurin, P.N. Single-ion fluorescence spectroscopy of a $Y_2SiO_5:Pr^{3+}$ nanocluster. *Phys. Lett. A* **2003**, *316*, 147–152.

2. Liu, G.H.; Chen, X.Y.; Zhuang, H.Z.; Li, S.; Niedbala, R.S. Confinement of electron–phonon interaction on luminescence dynamics in nanophosphors of Er^{3+}:Y_2O_2S. *J. Solid State Chem.* **2003**, *171*, 123–132.
3. Bednarkiewicz, A.; Mączka, M.; Strek, W.; Hanuza, J.; Karbowiak, M. Size dependence on infrared spectra of $NaGdF_4$ nanocrystals. *Chem. Phys. Lett.* **2006**, *418*, 75–78.
4. Meltzer, R.S.; Feofilov, S.P.; Tissue, B.; Yuan, H.B. Dependence of fluorescence lifetimes of Y_2O_3:Eu^{3+} nanoparticles on the surrounding medium. *Phys. Rev. B* **1999**, *60*, R14012–R14015.
5. Schmechel, R.; Kennedy, M.; Seggerm, H.V.; Winkler, H.; Kolbe, M.; Fischer, R.A.; Xaomao, L.; Benker, A.; Winterer, M.; Hahn, H. Luminescence properties of nanocrystalline Y_2O_3:Eu^{3+} in different host materials. *J Appl. Phys.* **2001**, *89*, 1679–1686.
6. Bednarkiewicz, A.; Strek, W. Laser-induced hot emission in Nd^{3+}/Yb^{3+}:YAG nanocrystallite ceramics. *J. Phys. D: Appl. Phys.* **2002**, *35*, 2503–2507.
7. Bednarkiewicz, A.; Mech, A.; Karbowiak, M.; Strek, W. Spectral properties of Eu^{3+} doped $NaGdF_4$ nanocrystals. *J. Luminescence* **2005**, *114*, 247–254.
8. Mehnaoui, M.; Panczer, G.; Ternane, R.; Trabelsi-Ayedi, M.; Boulon, G. Structural and spectroscopic characterizations in Pb^{2+}-doped calcium hydroxyapatites. *Opt. Mater.* **2008**, *30*, 1672–1676.
9. Fleet, M.E.; Pan, Y. Site preference of Nd in fluorapatite [$Ca_{10}(PO_4)_6F_2$]. *J. Solid State Chem.* **1994**, *112*, 78–81.
10. Ryan, F.M.; Warren, R.W.; Hopkins, R.H.; Murphy, J. *J. Electrochem. Soci.* **1978**, *125*, 1493–1498.
11. DeLoach, L.D.; Payne, S.A.; Chase, L.L.; Smith, L.K.; Kway, W.L.; Krupke, W.F. Evaluation of absorption and emission properties of Yb^{3+} doped crystals for laser applications. *IEEE J. Quantum Elect.* **1993**, *29*, 1179–1191.
12. DeLoach, L.D.; Payne, S.A.; Kway, W.L.; Tassano, J.B.; Dixit, S.N.; Krupke, W.F. Vibrational structure in the emission spectra of Yb^{3+}-doped apatite crystals. *J. Lumin.* **1994**, *62*, 85–94.
13. Spariosu, K.; Stultz, R.D.; Birnbaum, M.; Allik, T.H.; Hutchinson, J.A. Er:$Ca_5(PO_4)_3F$ saturable absorber Q switch for the Er:glass laser at 1.53 mM. *Appl. Phys. Lett.* **1993**, *62*, 2763–2765.
14. Kodaira, C.A.; Brito, H.F.; Malta, O.L.; Serra, O.A. Luminescence and energy transfer of the europium (III) tungstate obtained via the Pechini method. *J. Lumin.* **2003**, *101*, 11–21.
15. Sudarsanan, K.; Young, R.A. Significant precision in crystal structural details: Holly Springs hydroxyapatite. *Acta Crystallographica Section B* **1969**, *25*, 1534–1543.
16. Martin, P.; Carlot, G., Chevarier, A.; Den-Auwer, C.; Panczer, G. Mechanisms involved in thermal diffusion of rare earth elements in apatite. *J. Nucl. Mater.* **1999**, *275*(3), 268–276.
17. Zhang, H.; Ye, X.J.; Li, J.S. Preparation and biocompatibility evaluation of apatite/wollastonite-derived porous bioactive glass ceramic scaffolds. *Biomed. Mater.* **2009**, *4*, 045007.
18. Doat, A.; Pelle, F.; Gardant, N.; Lebugle, A. Synthesis of luminescent bioapatite nanoparticles for utilization as a biological probe. *J. Solid State Chem.* **2004**, *1777*, 1179–1187.
19. Silva, A.C.; Filho, F.P.; Sombra, A.S.B.; Rosa, I.L.V.; Leite, E.R.; Longo, E.; Varela, J.A. Study of Structural and Photoluminescent Properties of $Ca_8Eu_2(PO_4)_6O_2$. *J. Fluorescence* **2008**, *18*, 253–259.
20. Scherrer, P. Bestimmung der Grösse und der inneren Struktur von Kolloidteilchen mittels Röntgenstrahlen. *Goettinger Nachrichten* **1918**, *2*, 98–100.
21. El Ouenzer, R.; Kbir-Ariguib, N.; Trabelsi-Ayedi, M.; Piriou, B. Spectroscopic study of Eu^{3+} in strontium hydroxyapatite $Sr_{10}(PO_4)_6(OH)_2$. *J. Lumin.* **1999**, *85*, 71–77.
22. Ternane, R.; Trabelsi-Ayedi, M.; Kbir-Ariguib, N.; Piriou, B. Luminescent properties of Eu^{3+} in calcium hydroxyapatite. *J. Lumin.* **1999**, *81*, 165–170.
23. Piriou, B.; Fahmi, D.; Dexpert-Ghys, J.; Taitati, A.; Lacout, J.L. Unusual fluorescent properties of Eu^{3+} in oxyapatites. *J. Lumin.* **1987**, *39*, 97–103.
24. Kaminskii, A.A. *Crystalline Lasers: Physical Processes and Operating Schemes.* CRC Press: New York, **1996**, 267–268.
25. de Sa, G.F.; Malta, O.L.; de Mello Donega, C.; Simas, A.M.; Longo, R.L.; Santa-Cruz, P.A.; da Silva, Jr., E.F. Spectroscopic properties and design of highly luminescent lanthanide coordination complexes. *Coordination Chem. Rev.* **2000**, *196*, 165–195.
26. Kiliaan, H.S.; Kotte, J.F.A.K.; Blasse, G. Ultraviolet $^5H_3$ and visible ^5D_J luminescence of Europium(III) co-doped with cerium(III) in hexagonal $NaGdF_4$. *Chem. Phys. Lett.* **1987**, *133*, 425–428.